Journal of ELECTRONIC MATERIALS, Vol. 44, No. 1, 2015
DOI: 10.1007/s11664-014-3419-4

Transmission Electron Microscopy Study of $Mg_2Si_{0.5}Sn_{0.5}$ Solid Solution for High-Performance Thermoelectrics

JI-WEI LIU,[1] MINGHUI SONG,[1,4] MASAKI TAKEGUCHI,[1] NAOHITO TSUJII,[2] and YUKIHIRO ISODA[3]

1.—Nanocharacterization Group, Transmission Electron Microscopy Station, National Institute for Materials Science (NIMS), 1-2-1 Sengen, Tsukuba, Ibaraki 305-0047, Japan. 2.—Neutron Scattering Group, Quantum Beam Unit, NIMS, 1-2-1 Sengen, Tsukuba, Ibaraki 305-0047, Japan. 3.—Eco-energy Group, Battery Materials Unit, NIMS, 1-2-1 Sengen, Tsukuba, Ibaraki 305-0047, Japan. 4.—e-mail: minghui.song@nims.go.jp

A $Mg_2Si_{0.5}Sn_{0.5}$ solid solution was prepared by mixing Mg_2Si and Mg_2Sn powders and hot-pressing the mixture. The $Mg_2Si_{0.5}Sn_{0.5}$ samples exhibited a much lower thermal conductivity (1.92 W m^{-1} K^{-1} at 300 K) than the parent Mg_2Si (8.75 W m^{-1} K^{-1}) and Mg_2Sn compounds (6.28 W m^{-1} K^{-1}). X-ray diffraction measurements confirmed the successful synthesis of the $Mg_2Si_{0.5}Sn_{0.5}$ solid solution. Electron microscopy observations revealed that the grains were mainly 10–20 μm in size and had clean grain boundaries without obvious inclusions and precipitates. The major phase was cubic $Mg_2Si_{0.5}Sn_{0.5}$. MgO nanoparticles 10–20 nm in diameter were evenly dispersed in the $Mg_2Si_{0.5}Sn_{0.5}$ matrix, which probably reduced its thermal conductivity; moreover, uneven structures containing pure Si and Sn particles were found in the $Mg_2Si_{0.5}Sn_{0.5}$ grains. The origin and the formation mechanisms of the MgO and other impurity particles, and their effect on thermoelectric properties of $Mg_2Si_{0.5}Sn_{0.5}$, are discussed. The low thermal conductivity of $Mg_2Si_{0.5}Sn_{0.5}$ resulted in a relatively high dimensionless figure of merit ZT = 0.0132 at 300 K, which may be further increased by optimizing the synthesis procedure, alloy composition, and doping level. This work provides information on the structure and chemistry and their relationship with the thermoelectric properties of the $Mg_2Si_{0.5}Sn_{0.5}$ solid solution; it may help in developing other $Mg_2Si_{1-x}Sn_x$ compounds with superior thermoelectric properties.

Key words: $Mg_2Si_{0.5}Sn_{0.5}$, solid solution, microstructure, TEM, thermoelectric properties

INTRODUCTION

Thermoelectric materials are functional materials that can directly convert thermal energy to electricity and vice versa. With many features such as the absence of moving parts, low maintenance cost, long life, and high reliability, thermoelectric materials have received considerable attention due to their potential applications in power generation and solid-state refrigeration.[1–3] In general, the thermoelectric performance is evaluated in terms of a dimensionless figure of merit, $ZT = S^2\sigma T/\kappa$, where S, σ, T and κ are, respectively, the Seebeck coefficient, electrical conductivity, absolute temperature, and thermal conductivity that contains the electronic (κ_e) and lattice components (κ_l), respectively. To obtain a high ZT, it would be beneficial to increase the power factor ($S^2\sigma$) and/or decrease the thermal conductivity.[4]

Because of their good electrical properties, low lattice thermal conductivity, and potentially high ZT, intermetallic compounds of Mg_2X (X = Si, Sn or Ge) are promising thermoelectric materials in the

(Received June 21, 2014; accepted September 11, 2014; published online October 1, 2014)

intermediate temperature range (400–800 K).[5,6] These compounds are attractive for high-volume applications owing to their low toxicity, environmental friendliness, high abundance, and low production cost as compared to other state-of-the-art thermoelectric materials such as filled skutterudites and PbTe.[7–9] Mg_2X compounds exhibit semiconductor-like or semimetallic behaviors, and therefore most of the recent investigations have been focused on their solid solutions, aiming to decrease electrical resistivity and thermal conductivity.[10] For example, Zaitsev et al. investigated *n*-type $Mg_2Si_{1-x}Sn_x$ solid solutions in a broad range of compositions, and found that the large atomic mass difference between Si and Sn dramatically reduces the thermal conductivity of the solid solutions, which leads to a high *ZT* value of about 1.1 near 800 K.[11] However, it remains a challenge to fabricate homogeneous and stoichiometric $Mg_2Si_{1-x}Sn_x$ solid solutions because of the high vapor pressure, easy oxidation of Mg, and large differences in the melting points of Mg, Si, and Sn.[6,12] Moreover, as reported in many experimental and theoretical studies, the thermoelectric properties of these materials strongly depend on the local microstructure.[13–16] Accurate structural and chemical information is essential for improving the thermoelectric performance of the $Mg_2Si_{1-x}Sn_x$ solid solutions; however, detailed structural analyses of these materials are rare. Although it is widely accepted that the miscibility gap of $Mg_2Si_{1-x}Sn_x$ alloys exists between $x = 0.4$ and 0.6, it has been reported that solid solution phases such as $Mg_2Si_{0.5}Sn_{0.5}$ can be obtained in a certain synthesis process within this miscibility gap.[11,17] To date, Isoda et al. have reported the synthesis and thermoelectric properties of several $Mg_2Si_{1-x}Sn_x$ solid solutions with $x = 0.25$, 0.5 and 0.75.[18–21] For a systematic study of these materials, we performed a detailed structural analysis of a $Mg_2Si_{0.5}Sn_{0.5}$ solid solution using transmission electron microscopy (TEM) techniques in order to investigate the microstructure and its effect on thermoelectric properties. We believe that these results may be referable to the study of other $Mg_2Si_{1-x}Sn_x$ solid solutions.

EXPERIMENTAL PROCEDURES

The $Mg_2Si_{0.5}Sn_{0.5}$ solid solution was prepared by mixing Mg_2Si and Mg_2Sn powders and hot-pressing the mixture.

Table I summarizes some parameters of the starting materials for the synthesis of the Mg_2Si and Mg_2Sn powders. Mg_2Si alloys were synthesized by the liquid–solid reaction method.[18–21] Briefly, the elemental powders of Mg and Si were thoroughly mixed using an alumina mortar under an inert Ar atmosphere, and the mixture was then moved into a graphite crucible and subsequently heated in an electric furnace under an atmosphere of Ar + H_2(3%) at 1103 K for 2 h. Finally, the resulting alloys were allowed to cool to room temperature naturally. Mg_2Sn alloys were synthesized by the melting reaction method.[22,23] The starting materials including Mg and Sn were mixed, heated and cooled in the same way as that of the Mg and Si powders. The obtained Mg_2Si and Mg_2Sn ingots were then ground in an alumina mortar under Ar atmosphere. The resulted powders were sifted to select particles with diameters of 38–75 μm. The Mg_2Si and Mg_2Sn particles were then mixed and hot-pressed under Ar atmosphere at 80 MPa and 1068 K for 50 h. The relative density of the products was about 99% of the theoretical value of the stoichiometric $Mg_2Si_{0.5}Sn_{0.5}$. The hot-pressed ingots were cut into appropriate sizes using a diamond disk for further structural and thermoelectric measurements.

Measurements of thermoelectric properties, including Seebeck coefficient (S), electrical conductivity (σ), and thermal conductivity (κ), have been described previously.[18–22] Powder x-ray diffraction

Table I. Some parameters of the starting materials for the synthesis of the Mg_2Si and Mg_2Sn powders

Material	Purity	Shape	Molar ratio	Mole (mol)	Weight (g)
Mg	3 N	3–4 mm granule	2.024	0.43064	10.4668
Si	6 N	Powder	0.500	0.10637	2.9874
Sn	5 N	1 mm granule	0.500	0.10636	12.6262

Table II. Thermoelectric properties of $Mg_2Si_{1-x}Sn_x$ ($x = 0$, 0.5, 1) at 300 K

Material	Seebeck coefficient S (μV K^{-1})	Electrical conductivity σ (Ω^{-1} m^{-1})	Thermal conductivity κ (W m^{-1} K^{-1})	Figure of merit ZT	Carrier concentration n (m^{-3})
Mg_2Si	−397	1919	8.75	0.0104	9.1×10^{23}
$Mg_2Si_{0.5}Sn_{0.5}$	−574	256	1.92	0.0132	4.8×10^{23}
Mg_2Sn	−332	5525	6.28	0.0291	1.38×10^{24}

(XRD) patterns were recorded using a Bruker D8 x-ray diffractometer with Ni-filtered Cu K_α radiation (40 kV, 40 mA). The size and morphology of the products were characterized by a field-emission scanning electron microscope (SEM; JSM-7000F; JEOL). Selected-area electron diffraction (SAED), TEM, high-resolution TEM (HRTEM), low-angle and high-angle annular dark-field scanning TEM (LAADF/HAADF-STEM), and energy dispersive x-ray spectroscopy (EDS) measurements were performed on a JEOL JEM-2100F transmission electron microscope at an accelerating voltage of 200 kV. LAADF/HAADF-STEM images were acquired with a camera length of 20 cm/8 cm and collection angles of 30–80 mrad/85–210 mrad. EDS analysis was performed in the STEM mode with an electron probe of 1 nm in diameter. TEM specimens were prepared in two ways. One was the FIB method, by which thin film specimens were cut directly from bulk materials with a focused ion beam system (FIB; JIB-4000; JEOL) using a 30 keV Ga^+ ion beam. A carbon layer in thickness larger than 500 nm was deposited on the top surface of the bulk materials to pretect the surface from the Ga^+ ion irradiation before the FIB machining. Another way was to crush bulk materials to powders in an alumina mortar under Ar atmosphere at room temperature. The obtained powders were dispersed in ethanol and then dropped onto a polymer microgrid supported by a copper frame. All the TEM specimens were preserved in a vacuum chamber and then transferred into the TEM column for observation within 12 h.

RESULTS AND DISCUSSION

The measured values of S, σ, and κ are listed in Table II. $Mg_2Si_{0.5}Sn_{0.5}$ has a negative S, indicating n-type conduction. Its $|S|$ value is larger and κ is lower than those of Mg_2Si and Mg_2Sn, which are favorable for thermoelectric applications. Because of its relatively low σ, the figure of merit ZT for $Mg_2Si_{0.5}Sn_{0.5}$ is small (0.0132 at 300 K), which is a little higher than that of Mg_2Si (0.0104), but less than half that of Mg_2Sn (0.0291). The main reason for the low σ of $Mg_2Si_{0.5}Sn_{0.5}$ is considered to be the much lower carrier concentration compared to that of Mg_2Sn. The carrier concentration of $Mg_2Si_{0.5}Sn_{0.5}$ can be increased by appropriate doping and therefore the ZT value is expected to be improved.[6,18]

The crystal structure and phase purity of the products were characterized by XRD. It is known that Mg_2Si, Mg_2Sn, and their alloys crystallize in the antifluorite structure with Si or Sn atoms located in the face-centered cubic positions and Mg atoms occupying the tetrahedral sites (inset in Fig. 1). Figure 1 shows the XRD pattern of the $Mg_2Si_{0.5}Sn_{0.5}$ compound. All identified diffraction peaks lie between those of Mg_2Si (JCPDS card no. 35-0773) and Mg_2Sn (JCPDS card no. 65-2997). The lattice constant for the cubic unit cell was

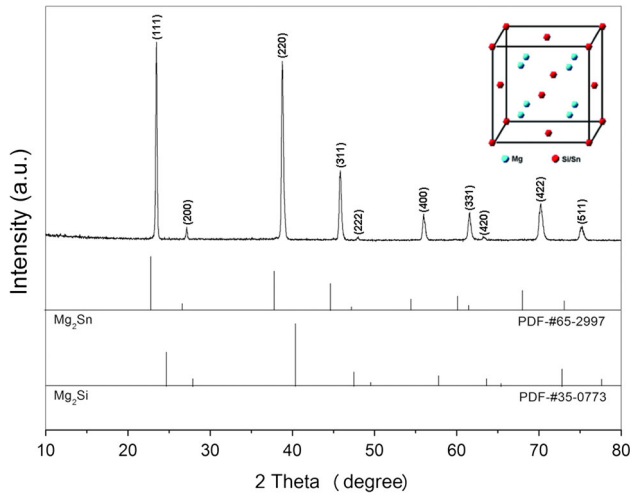

Fig. 1. XRD pattern of the $Mg_2Si_{0.5}Sn_{0.5}$ compound. *Inset* the crystal structure of antifluorite compounds Mg_2X (X = Si or/and Sn).

determined as a = 6.545 Å, which is intermediate between those of Mg_2Si (6.351 Å) and Mg_2Sn (6.759 Å). No peaks associated with Mg, Si, Sn, Mg_2Si or Mg_2Sn phases were detected, indicating the successful synthesis of the antifluorite structure phase of Mg_2Si, Mg_2Sn solid solution.

The size, morphology, and microstructure of $Mg_2Si_{0.5}Sn_{0.5}$ samples were investigated by SEM and TEM. As shown in Fig. 2, the grain size is mostly 10–20 μm and the grain boundaries contain no obvious inclusions or precipitates. Figure 3a shows a representative bright-field (BF) TEM image of the $Mg_2Si_{0.5}Sn_{0.5}$ specimen. The SAED pattern (Fig. 3b), HRTEM image (Fig. 3c), and the corresponding fast Fourier transform (FFT) pattern (Fig. 3d) indicate that the material is of high crystallinity. The measured interplanar spacings of ~0.38 nm and ~0.33 nm correspond to the {111} and {200} planes of cubic $Mg_2Si_{0.5}Sn_{0.5}$, respectively. In all cases, SAED patterns show that $Mg_2Si_{0.5}Sn_{0.5}$ solid solution is the major phase, which is consistent with the XRD results. Rings characteristic of randomly oriented crystallites were detected in some SAED patterns (Fig. 4b) and identified as cubic MgO (JCPDS card no. 45-0946). The dark-field (DF) TEM image acquired by selecting a part of MgO SAED ring revealed evenly dispersed MgO nanoparticles 10–20 nm in size (Fig. 4c). We prepared the TEM specimens by FIB at grains in size of 10–20 μm. Since the thickness of the TEM specimen (~100 nm) is about two orders of magnitude smaller than the grain size, these MgO nanoparticles may not be on the grain boundary but be embedded in the grains. We also observed these dispersed MgO nanoparticles in the TEM specimens prepared by dispersing the crushed powder in ethanol and dropping onto a microgrid, as shown in Fig. 5. Therefore, these MgO nanoparticles may not be the artifacts from the FIB process. The SAED pattern in

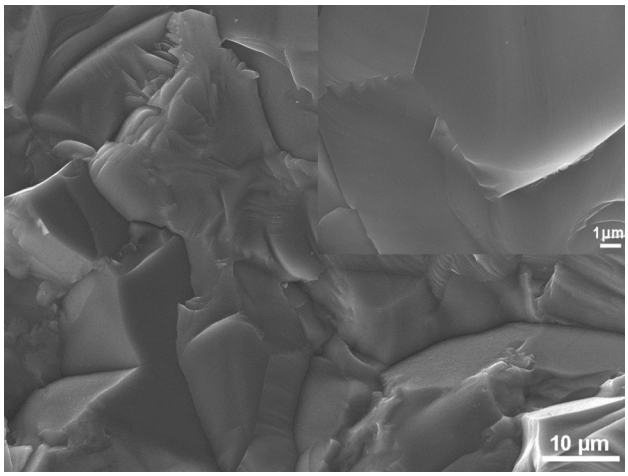

Fig. 2. SEM image of the $Mg_2Si_{0.5}Sn_{0.5}$ compound.

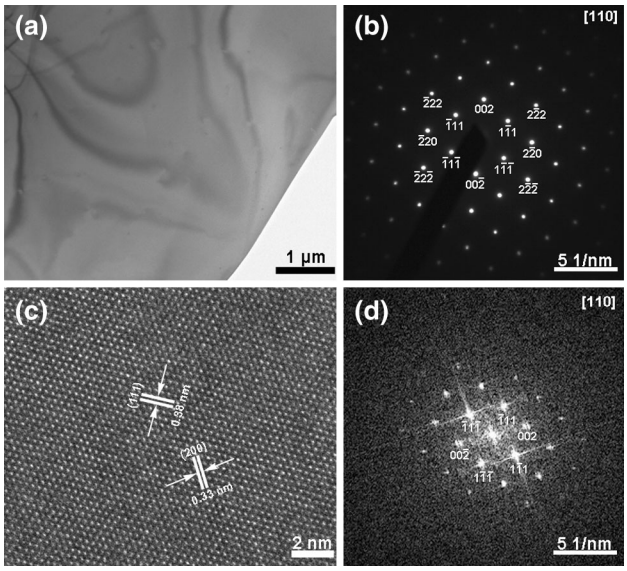

Fig. 3. (a) BF-TEM image of the $Mg_2Si_{0.5}Sn_{0.5}$ specimen, (b) SAED pattern, (c) HRTEM image, and (d) corresponding FFT pattern of (c).

Fig. 5b is similar to that in Fig. 4b. However, by observing Fig. 5b carefully, it can be found that there are some bright diffraction dots in the SAED rings of MgO. Figure 5c shows the DF-TEM image acquired by selecting a part of the diffraction ring of MgO (200), where there are fewer bright dots. The obtained DF-TEM image is similar to that in Fig. 4c. Figure 5d also shows a DF-TEM image acquired by selecting a part of the diffraction ring of MgO (200), where there are more bright dots. The obtained DF-TEM image shows dispersed MgO nanoparticles in size of 10∼20 nm, as well as some larger MgO nanoparticles at a size of about 30 nm. As shown in Fig. 5a, the larger nanoparticles can be clearly observed in the BF-TEM image. It is possible that these larger MgO nanoparticles may be distributed on the grain boundary. These results confirmed again that TEM specimen preparation methods of both FIB and crushing have their advantages and disadvantages. With FIB, a position can be selected in accuracy smaller than 100 nm to prepare a TEM specimen with uniform thickness. Therefore, a typical position within a grain or grain boundary can definitely be observed. However, FIB may introduce artifacts due to the irradiation by Ga ions. Also, if the density of a feature, such as the second phase particles, is not high enough, the feature may be difficult to be confirmed on the boundary. On the other hand, crushing is a simple method and most likely to reveal the original structure and composition of a specimen. However, if the distribution of a featured structure is not even in a specimen, it may be difficult to get precise and overall information of the specimen. To comprehensively identify the structure of a specimen, it is better to combine these two methods.

STEM was employed to further identify the local chemical composition. Figure 6a and b, respectively, show the LAADF and HAADF STEM images of the $Mg_2Si_{0.5}Sn_{0.5}$ specimen, indicating the homogeneity of its grains. According to the semi-quantitative composition analysis, the atomic ratio of Mg:Si:Sn is nearly 4:1:1 (Fig. 6c). The EDS spectrum also shows

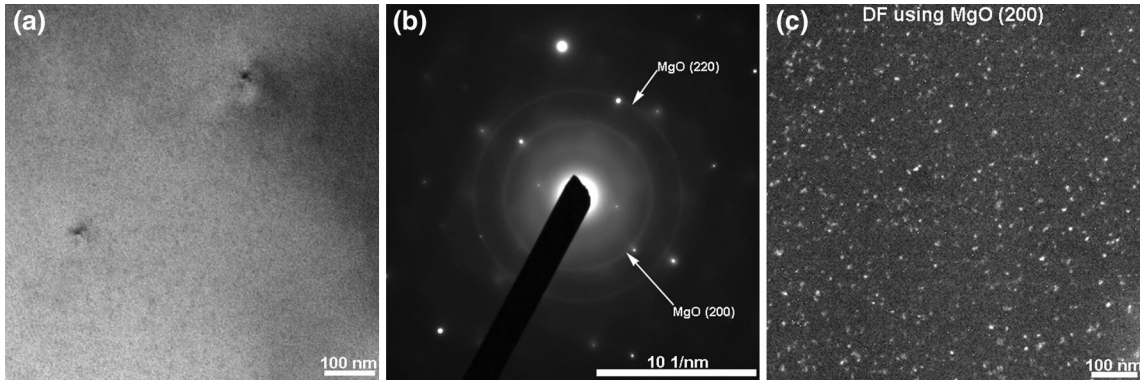

Fig. 4. (a) BF-TEM image and (b) SAED pattern of the $Mg_2Si_{0.5}Sn_{0.5}$ specimen prepared by FIB. (c) DF-TEM image acquired using a part of the (200) diffraction ring of MgO.

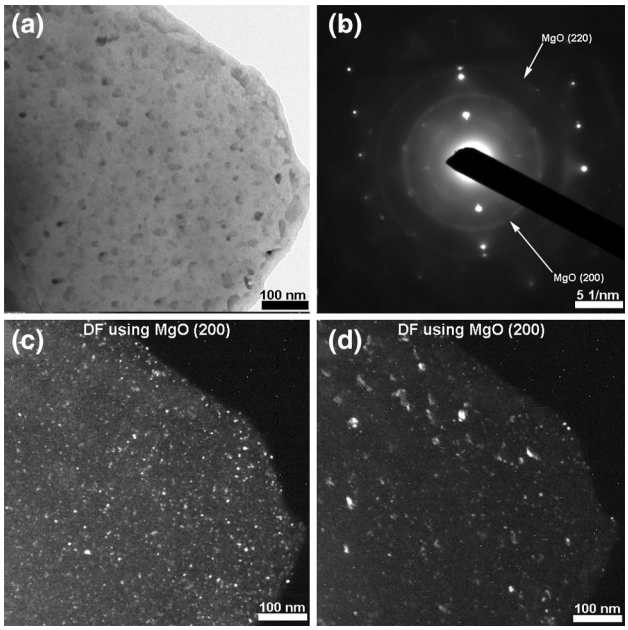

Fig. 5. (a) BF-TEM image and (b) SAED pattern of the $Mg_2Si_{0.5}Sn_{0.5}$ specimen prepared by dispersing the powder in ethanol and dropping onto a microgrid. (c) DF-TEM image acquired using a part of the (200) diffraction ring of MgO, where there are fewer bright dots. (d) DF-TEM image acquired using a part of the (200) diffraction ring of MgO, where there are more bright dots.

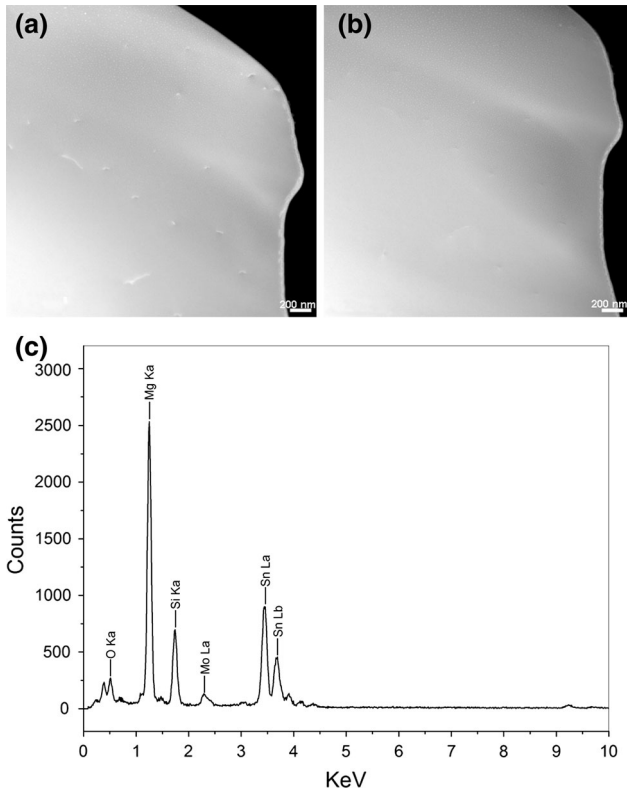

Fig. 6. (a) LAADF-STEM image, (b) HAADF-STEM image, and (c) corresponding EDS spectrum of the $Mg_2Si_{0.5}Sn_{0.5}$ specimen. Mo signals in the spectrum originate from the molybdenum mesh supporting the FIB specimen.

a small amount of oxygen, which can be attributed to the MgO phase in the $Mg_2Si_{0.5}Sn_{0.5}$ matrix.

Some uneven structures were found in the $Mg_2Si_{0.5}Sn_{0.5}$ grains (Fig. 7a). The contrast in this BF-TEM image revealed two kinds of areas, denoted as A and B, which were further characterized by SAED and DF-TEM. SAED pattern (Fig. 7b) and corresponding DF-TEM image (Fig. 7c) revealed that the major phase in the A-area is similar to $Mg_2Si_{0.5}Sn_{0.5}$ solid solution as shown in Fig. 3. Polycrystalline rings were also detected in A-area SAED patterns (Fig. 8b) and identified as cubic Si (JCPDS card no. 27-1402) and MgO. DF-TEM images confirmed the presence of Si and MgO as minor phases (Fig. 8c and d). The particles with a diameter of ~100 nm are Si particles and the evenly dispersed ones with diameters of 10–20 nm are MgO nanoparticles. Figure 7d shows the SAED pattern of the B-area, which can be indexed by two tetragonal Sn crystals (C1, C2) parallel in (01-1) plane (JCPDS card no. 04-0673). DF-TEM imaging confirmed the existence of crystalline Sn several hundreds of nanometers in size (Fig. 7e). As shown in Fig. 9, both Si and MgO particles also exist in the B-area. It is worth mentioning that these MgO, Si, and Sn particles could not be detected by XRD, indicating their low volume fraction. To check the stability of the $Mg_2Si_{0.5}Sn_{0.5}$ solid solution, a part of the as-prepared products were further annealed at 1073 K for 250 h. No phase separation was observed by XRD measurement and TEM observation, indicating that the $Mg_2Si_{0.5}Sn_{0.5}$ solid solution may be reasonably stable if it is utilized at temperature below eutectic point.

Detailed characterization revealed that the major phase of the synthesized product was $Mg_2Si_{0.5}Sn_{0.5}$ solid solution with a small amount of MgO nanoparticles evenly dispersed in the matrix. While the presence of MgO in $Mg_2Si_{1-x}Sn_x$ has been documented,[24–28] this is the first report of evenly dispersed MgO nanoparticles in the $Mg_2Si_{0.5}Sn_{0.5}$ solid solution, to the best of our knowledge. The formation of these MgO nanoparticles could be interpreted mainly in two ways: (1) oxygen may exist in the starting materials and cause the formation of MgO particles; and (2) oxygen may originate from the trace volume in the Ar atmosphere of the synthesis processes and form a thin MgO film on the surface of the products. These MgO particles or thin MgO film may be crushed and mixed into the powders during the mixing process. In addition, the subsequent hot-pressing process was performed at 1068 K. This temperature is lower than the melting point of Mg_2Si (1219 K) and close to that of Mg_2Sn (1048 K),[25] at which the alloying of $Mg_2Si_{0.5}Sn_{0.5}$ may be partially processed in solid state. Therefore, not all the MgO nanoparticles were separated out from the matrix and segregated on the grain boundary, but some of them may be embedded in the grain. We also detected some uneven structures

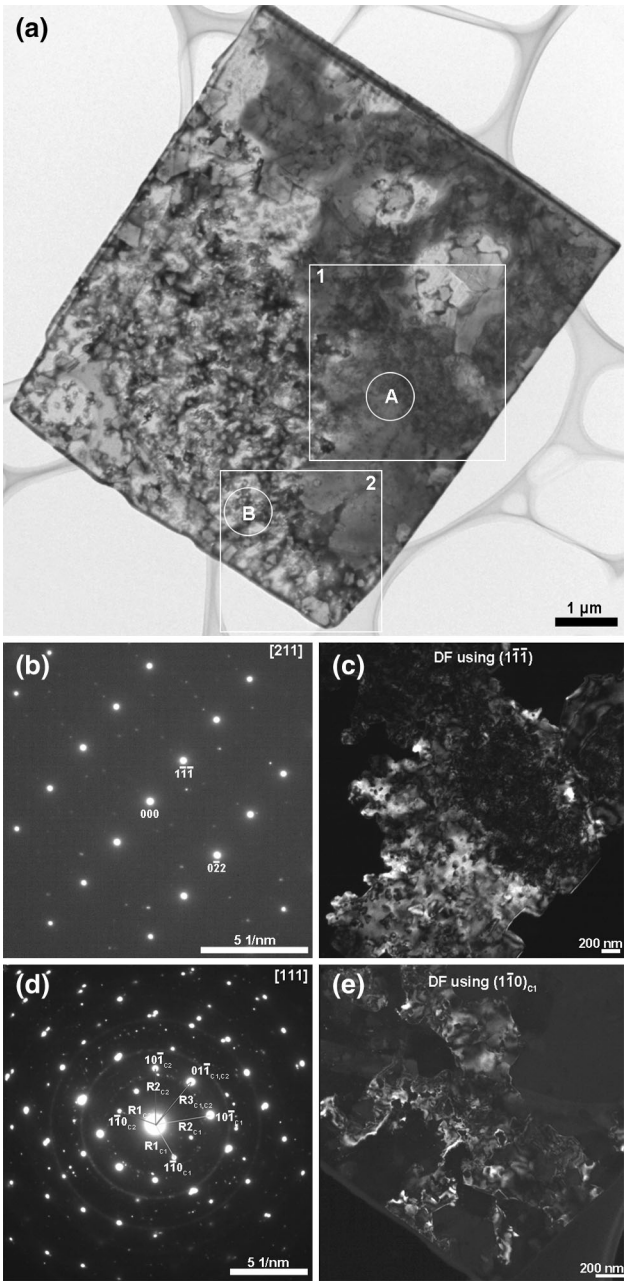

Fig. 7. (a) BF-TEM image of the uneven structures in the grain of the $Mg_2Si_{0.5}Sn_{0.5}$ specimen. (b) SAED pattern of the *A*-area indicated in (a). (c) DF-TEM image of area 1 in (a) acquired using the (1$\bar{1}\bar{1}$) diffraction spot of $Mg_2Si_{0.5}Sn_{0.5}$. (d) SAED pattern of the *B*-area indicated in (a). (e) DF-TEM image of area 2 in (a) acquired using the (1$\bar{1}$0)$_{C1}$ diffraction spot of Sn.

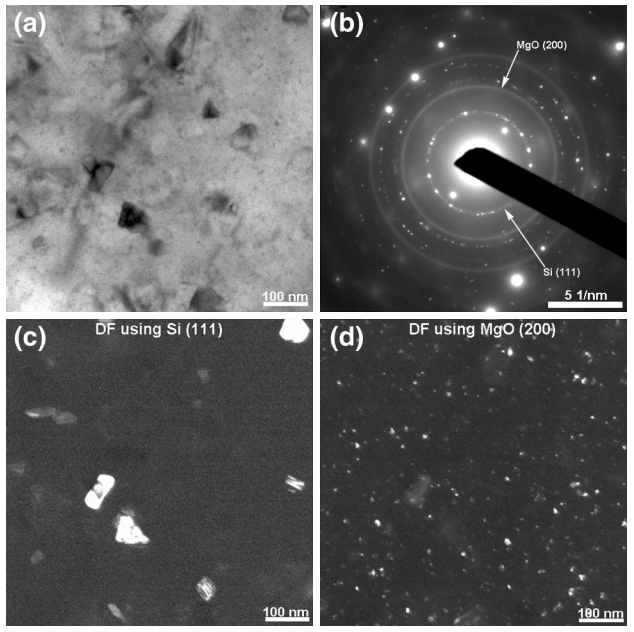

Fig. 8. (a) BF-TEM image and (b) SAED pattern of the *A*-area (in Fig. 7) in the $Mg_2Si_{0.5}Sn_{0.5}$ specimen. (c) DF-TEM image acquired using a part of the (111) diffraction ring of Si. (d) DF-TEM image acquired using a part of the (200) diffraction ring of MgO.

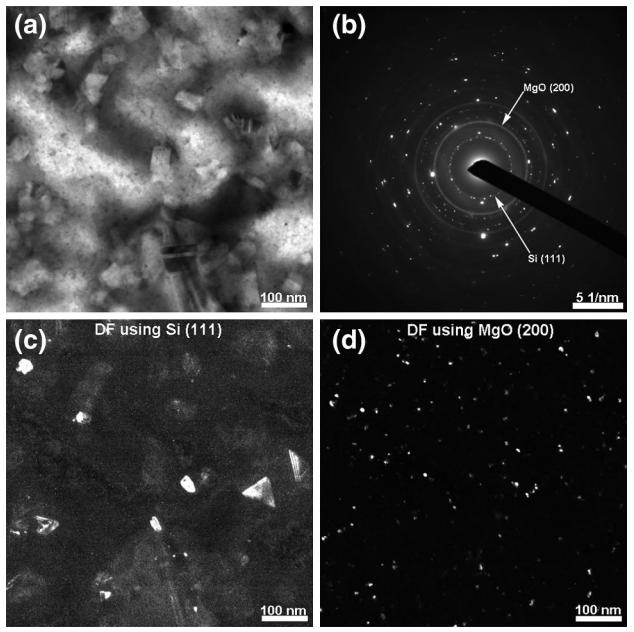

Fig. 9. (a) BF-TEM image and (b) SAED pattern of the *B*-area (in Fig. 7) in the $Mg_2Si_{0.5}Sn_{0.5}$ specimen. (c) DF-TEM image acquired using a part of the (111) diffraction ring of Si. (d) DF-TEM image acquired using a part of the (200) diffraction ring of MgO.

containing pure Si and Sn particles in the $Mg_2Si_{0.5}Sn_{0.5}$ grains. Although Mg was added in 5 mol% excess of stoichiometric amounts, it is most likely that the Mg content in the alloys was deficient because of the high vapor pressure of Mg. The Mg might have been lost due to evaporation during the synthesis process, resulting in the formation of residual Si and Sn phases.[6,24] Recent experiments and calculations have confirmed that nanostructures embedded in a bulk matrix may provide an additional scattering mechanism for the mid- and long-wavelength phonons, thereby reducing the lattice thermal conductivity.[14,29–31] Thus, the evenly dispersed MgO nanoparticles could reduce κ of the $Mg_2Si_{0.5}Sn_{0.5}$ solid solution via phonon scattering,

but they might also scatter the charge carriers and reduce the electrical conductivity σ. A further investigation is necessary to understand the impact of nanosized MgO on the ZT value.[17,32] As for the uneven structures containing pure Si and Sn particles, it is especially important to prevent these phase separations during the synthesis to obtain a homogeneous $Mg_2Si_{0.5}Sn_{0.5}$ solid solution in high yield. A further increase in the ZT values by optimizing the synthesis procedure, alloy composition, and doping level is a promising avenue for improving the thermoelectric properties of $Mg_2Si_{1-x}Sn_x$ solid solutions for practical applications.

CONCLUSIONS

We performed a detailed structural analysis of the $Mg_2Si_{0.5}Sn_{0.5}$ solid solution prepared by mixing Mg_2Si and Mg_2Sn powders and hot-pressing the mixture. XRD measurements confirmed the formation of the $Mg_2Si_{0.5}Sn_{0.5}$ solid solution. SEM images showed grains 10-20 μm in size with clean grain boundaries. TEM and STEM analyses revealed that cubic $Mg_2Si_{0.5}Sn_{0.5}$ was the major phase. Minor MgO, Si, and Sn inclusions were also identified, which could not be detected by XRD, with MgO nanoparticles 10–20 nm in size being evenly dispersed in the $Mg_2Si_{0.5}Sn_{0.5}$ matrix. The nearly single-phase composition and the presence of MgO nanoparticles might explain the very low thermal conductivity and relatively high ZT value of the $Mg_2Si_{0.5}Sn_{0.5}$ solid solution. Studies are currently underway to further increase the ZT values by optimizing the synthesis procedure, alloy composition, and doping level using a combination of doping and nanostructuring approach.

CONFLICT OF INTEREST

The authors declare that they have no conflict of interest.

REFERENCES

1. F.J. Di Salvo, *Science* 285, 703 (1999).
2. L.E. Bell, *Science* 321, 1457 (2008).
3. G.J. Snyder and E.S. Toberer, *Nature Mater.* 7, 105 (2008).
4. Y.C. Lan, A.J. Minnich, G. Chen, and Z.F. Ren, *Adv. Funct. Mater.* 20, 357 (2010).
5. M.I. Fedorov, *J. Thermoelectr.* 2, 51 (2009).
6. W. Liu, X.F. Tang, H. Li, J. Sharp, X.Y. Zhou, and C. Uher, *Chem. Mater.* 23, 5256 (2011).
7. R.C. Mallik, R. Anbalagan, K.K. Raut, A. Bali, E. Royanian, E. Bauer, G. Rogl, and P. Rogl, *J. Phys.: Condens. Matter* 25, 105701 (2013).
8. J.Q. He, L.D. Zhao, J.C. Zheng, J.W. Doak, H.J. Wu, H.Q. Wang, Y. Lee, C. Wolverton, M.G. Kanatzidis, and V.P. Dravid, *J. Am. Chem. Soc.* 135, 4624 (2013).
9. J.R. Sootsman, D.Y. Chung, and M.G. Kanatzidis, *Angew. Chem. Int. Ed.* 48, 8616 (2009).
10. H. Ihou-Mouko, C. Mercier, J. Tobola, G. Pont, and H. Scherrer, *J. Alloys Compd.* 509, 6503 (2011).
11. V.K. Zaitsev, M.I. Fedorov, E.A. Gurieva, I.S. Eremin, P.P. Konstantinov, A.Y. Samunin, and M.V. Vedernikov, *Phys. Rev. B* 74, 045207 (2006).
12. W. Liu, X.F. Tang, H. Li, K. Yin, J. Sharp, X.Y. Zhou, and C. Uher, *J. Mater. Chem.* 22, 13653 (2012).
13. B. Poudel, Q. Hao, Y. Ma, Y.C. Lan, A. Minnich, B. Yu, X.A. Yan, D.Z. Wang, A. Muto, D. Vashaee, X.Y. Chen, J.M. Liu, M.S. Dresselhaus, G. Chen, and Z.F. Ren, *Science* 320, 634 (2008).
14. C.J. Vineis, A. Shakouri, A. Majumdar, and M.G. Kanatzidis, *Adv. Mater.* 22, 3970 (2010).
15. X.J. Tan, W. Liu, H.J. Liu, J. Shi, X.F. Tang, and C. Uher, *Phys. Rev. B* 85, 205212 (2012).
16. J.Q. He, J. Androulakis, M.G. Kanatzidis, and V.P. Dravid, *Nano Lett.* 12, 343 (2012).
17. L.X. Chen, G.Y. Jiang, Y. Chen, Z.L. Du, X.B. Zhao, T.J. Zhu, J. He, and T.M. Tritt, *J. Mater. Res.* 26, 3038 (2011).
18. Y. Isoda, T. Nagai, H. Fujiu, Y. Imai, and Y. Shinohara, *Proceedings of the 26th International Conference on Thermoelectrics* (2007), p. 251.
19. Y. Isoda, S. Tada, T. Nagai, H. Fujiu, and Y. Shinohara, *J. Electron. Mater.* 39, 1531 (2010).
20. S. Tada, Y. Isoda, H. Udono, H. Fujiu, S. Kumagai, and Y. Shinohara, *J. Electron. Mater.* 43, 1580 (2014).
21. Y. Isoda, M. Held, S. Tada, and Y. Shinohara, *J. Electron. Mater.* 43, 2053 (2014).
22. Y. Isoda, N. Shioda, H. Fujiu, Y. Imai, and Y. Shinohara, *Proceedings of the 23rd International Conference on Thermoelectrics* (2005), p. 496.
23. S.M. Choi, T.H. An, W.S. Seo, C. Park, I.H. Kim, and S.U. Kim, *J. Electron. Mater.* 41, 1071 (2012).
24. G.S. Nolas, D. Wang, and M. Beekman, *Phys. Rev. B* 76, 235204 (2007).
25. Q. Zhang, J. He, X.B. Zhao, S.N. Zhang, T.J. Zhu, H. Yin, and T.M. Tritt, *J. Phys. D Appl. Phys.* 41, 185103 (2008).
26. Q. Zhang, J. He, T.J. Zhu, S.N. Zhang, X.B. Zhao, and T.M. Tritt, *Appl. Phys. Lett.* 93, 102109 (2008).
27. W. Liu, X.F. Tang, and J. Sharp, *J. Phys. D Appl. Phys.* 43, 085406 (2010).
28. T. Dasgupta, C. Stiewe, A.J. Zhou, L. Boettcher, and E. Mueller, *Phys. Rev. B* 83, 235207 (2011).
29. S. Wang and N. Mingo, *Appl. Phys. Lett.* 94, 203109 (2009).
30. X.B. Zhao, S.H. Yang, Y.Q. Cao, J.L. Mi, Q. Zhang, and T.J. Zhu, *J. Electron. Mater.* 38, 1017 (2009).
31. Z.L. Du, G.Y. Jiang, Y. Chen, H.L. Gao, T.J. Zhu, and X.B. Zhao, *J. Electron. Mater.* 41, 1222 (2012).
32. M. Saleemi, M.S. Toprak, S. Fiameni, S. Boldrini, S. Battiston, A. Famengo, M. Stingaciu, M. Johnsson, and M. Muhammed, *J. Mater. Sci.* 48, 1940 (2013).